

From an organometallic monolayer to an organic monolayer covered by metal nanoislands: a simple thermal protocol for the fabrication of the top contact electrode in molecular electronic devices

*Luz M. Ballesteros, Santiago Martín, Javier Cortés, Santiago Marqués-González, Francesc Pérez-Murano, Richard J. Nichols, Paul J. Low, and Pilar Cea**

Dr. L. M. Ballesteros, Dr. S. Martín, J. Cortés, Dr. P. Cea
Departamento de Química Física, Facultad de Ciencias Universidad de Zaragoza, Zaragoza, 50009, Spain

Dr. L. M. Ballesteros, J. Cortés, Dr. P. Cea
Instituto de Nanociencia de Aragón (INA) Campus Rio Ebro Edificio i+d Universidad de Zaragoza, Zaragoza, 50018, Spain.

Dr. S. Martín
Instituto de Ciencia de Materiales de Aragón (ICMA) Universidad de Zaragoza-CSIC, Zaragoza, 50009, Spain

S. Marqués-González, Prof. P. J. Low
Department of Chemistry University of Durham, Durham, DH1 3LE, United Kingdom

Prof. F. Pérez-Murano
Instituto de Microelectrónica de Barcelona (IMB-CNM, CSIC) Campus UAB, Bellaterra, 08193, Spain

Prof. R. J. Nichols
Department of Chemistry University of Liverpool, Liverpool, L69 7ZD, United Kingdom
Prof. P. J. Low

School of Chemistry and Biochemistry University of Western Australia, Perth, 6009, Australia

Dr. P. Cea
Laboratorio de Microscopias Avanzadas (LMA), Campus Rio Ebro Edificio i+d Universidad de Zaragoza, Zaragoza, 50018, Spain
E-mail: pilarcea@unizar.es

Keywords: Langmuir-Blodgett films; top-contact electrode; molecular junction

The continued societal and industrial demand for smaller, quicker, and more efficient electronic devices maintains sufficient economic pressure to drive Moore's Law based scaling of electronic circuits. However, the intrinsic financial and technological limitations in top-down scaling of conventional solid-state silicon technology^[1-2] have begun to demand consideration of alternative technologies and design concepts. Alongside More than Moore style device packaging,^[3-4] and revolutionary component designs^[5-6] the use of functional

organic molecules as basic components in electronic devices, i.e., molecular electronics, is gaining support as an alternative future technology.^[7-12] Although the immense opportunities offered by synthetic chemistry together with the sophisticated methods that allow the assembly of single molecules and assemblies of molecules onto solid supports with a high degree of control are promising for the development of molecular electronics, there are also some significant challenges before this technology can begin and journey towards the market. Among these challenges, the deposition of the top-contact electrode on monomolecular layers of active molecular components (see an illustrative example of a bottom electrode | monolayer | or top contact electrode in **Scheme I**) is of particular relevance to the assembly of device structures, as opposed to test junctions which can be formed in nanofabrication or scanning probe microscopy (SPM) based platforms.^[7, 13-15] Consequently, the metallization of monolayers has been the objective of intensive investigations in the last decades, and some excellent reviews have summarized the most important methods developed to date highlighting their advantages and limitations.^[7, 14, 16-18] As evidenced in these reviews, despite intense investigations on this topic a reliable control in the fabrication of molecular junctions remains rather limited. The main problems in the deposition of the second or top contact electrode are related to damage of the functional molecules during the metallization of the monolayer or penetration of the second metal through the organic films, which results in a short circuit, rendering the device unusable.^[7, 14, 16-17]

Recently, Chico et al.^[19] have reported the generation of a dispersion of metallic gold nanoparticles (GNPs) by thermal annealing of a metal organic compound (MOC) in solution, where the GNPs are stabilized by the organic counterparts of the pristine material. A thermal annealing strategy is also implemented in this contribution for the generation of the top metallic electrode. However, the chemical reaction to produce the gold nanoislands (GNIs) on the monolayer surface has been carried out after the MOC had been immobilized on a substrate. In this contribution different substrates have been used depending on the

characterization technique employed. As it will be demonstrated throughout the paper the thermal decomposition of the organometallic film is a general phenomenon that occurs independently of the substrate where the monolayer was immobilized, although for applications in the field of molecular electronics a bottom electrode or conductive substrate is required. Two different organometallic gold complexes [[4-(4-carboxy)ethynyl}phenyl]ethynyl)-(triphenylphosphine)-gold, **1**, and [1-isocyano-4-methoxybenzene]-[4-amino-phenylethynyl]-gold, **2** (**Scheme I**) were incorporated into well-ordered monomolecular films by the Langmuir-Blodgett (LB) technique since the LB method permits the fabrication of directionally oriented films,^[20-21] which is of vital importance to carry out the strategy presented for the fabrication of the top electrode in this paper. Thermal annealing of monomolecular LB films of these organometallic compounds causes the rupture of the P-Au-C or C-Au-C bonds and reduction of Au(I) to Au(0) as metallic GNIs that remain immobilized on the surface of the organic monolayer. Scheme I illustrates the processes that will be demonstrated to occur upon thermally induced decomposition of an organometallic compound, abbreviated as the TIDOC method.

Details about the experimental procedure to prepare and characterise the monolayers can be found in the supporting information (SI). These Langmuir films were transferred onto mica (AFM experiments), glass (XPS and contact angle measurements), quartz (UV-vis), and gold (c-AFM) solid supports. In all cases, the optimum surface pressure of transference for compound **1** is $10 \text{ mN}\cdot\text{m}^{-1}$ for which transfer ratios^[22] close to 1 were obtained (see SI). The area per molecule for **1** at this surface pressure, $0.33 \text{ nm}^2\cdot\text{molecule}^{-1}$, is in excellent agreement with the theoretical area per **1** unit, $0.32 \text{ nm}^2\cdot\text{molecule}^{-1}$, according to molecular models (Spartan[®] 08 V 1.0.0). A systematic study in which the surface supported LB films were annealed at different temperatures and during different periods of time was performed (see SI). The optimized results for compound **1** were obtained after an annealing process of 2 hours at $150 \text{ }^\circ\text{C}$, and subsequent washing and drying steps.

The processes taking place upon annealing were studied by a variety of methods. Initial annealing studies were carried out on films of **1** immobilised on a quartz crystal microbalance (QCM) resonator. The frequency change (Δf) for a QCM quartz resonator before and after the annealing process was determined. The Sauerbrey equation establishes that:^[23]

$$\Delta f = -\frac{2 \cdot f_0^2 \cdot \Delta m}{A \cdot \rho_q^{1/2} \cdot \mu_q^{1/2}} \quad (1)$$

where f_0 is the fundamental resonant frequency of 5 MHz, $\Delta m(g)$ is the mass change, A is the electrode area, ρ_q is the density of the quartz ($2.65 \text{ g}\cdot\text{cm}^{-3}$), and μ_q is the shear module ($2.95 \cdot 10^{11} \text{ dyn}\cdot\text{cm}^{-2}$). The surface coverage of the organic monolayer is $5.5 \cdot 10^{-10} \text{ mol}\cdot\text{cm}^{-2}$ as obtained from equation 1 considering the frequency variation before and after deposition of the monolayer. A variation of 14 Hz in the frequency after the annealing and subsequent rinsing process with chloroform was obtained. If it is assumed that the surface coverage of the organic monolayer is maintained after the annealing, washing and drying processes, this frequency change of 14 Hz is in good agreement with a loss of material of 262 amu, i.e., the molecular weight corresponding to the triphenyl phosphine (PPh₃) ligand.

Figure 1 shows the XPS spectra of pristine and annealed LB films of **1** on glass (glass was used to avoid any misinterpretation of the results by using a gold conductive substrate). The characteristic energy of phosphorus in the XPS spectrum provides a useful signal that can be used to follow the annealing process. As shown in Figure 1, the characteristic phosphorus peak which is present in the pristine films of **1** disappears after the annealing and subsequent rinsing process, indicating that the triphenylphosphine (PPh₃) group of **1** is lost after the thermal treatment. In addition, the Au4f region for the film after the annealing process shows two peaks at 83.81 and 87.48 eV, attributable to Au(0)^[24-26] whilst the pristine monolayer shows two intense peaks at 85.04 and 88.74 eV, attributable to Au(I),^[27-28] and two weaker peaks at 83.88 and 87.56 eV attributable to Au(0) that is probably formed during the irradiation process necessitated for recording the XPS spectrum.

These results clearly show that, after the thermal annealing and rinsing of the film, the PPh_3 group is removed and $\text{Au}(0)$ is obtained. It is important to verify if the thermally induced rupture of the Au-supporting ligand (L) bond is a general property of this family of compound $\text{Au}\{(\text{C}\equiv\text{CC}_6\text{H}_4)_n\text{R}\}\text{L}$ and not just a feature unique to compound **1**. Thus, a comprehensive study of **2** has also been performed (see SI for details of LB film preparation and characterization, and optimization of annealing conditions (100 °C, 2 hrs)). Again, the XPS spectra of the Au4f region confirms the reduction of $\text{Au}(\text{I})$ to $\text{Au}(0)$ once the film has been thermally annealed (see SI). In addition, for compound **2** it is also possible to discern by XPS that the isocyanide ligand is removed after the annealing and subsequent rinsing. Thus the XPS spectrum of **2** in powder shows a peak at 399.0 eV in the N1s spectral region attributable to the isocyanide group.^[29-31] This peak can also be observed in pristine LB films of **2** but disappears in the annealed films. Further evidence of the elimination of the isocyanide group after the thermal annealing and rinsing processes, is provided by the variation in the resonance frequency of a QCM substrate modified by pristine and subsequently annealed and rinsed LB films of **2**. After thermal annealing of the monolayer under the optimal conditions, thorough rinsing with chloroform and drying, the difference in resonance frequency of the monolayer (surface coverage, Γ , of $7.5 \cdot 10^{-10} \text{ mol}\cdot\text{cm}^{-2}$ determined with the QCM as detailed in the SI), with respect to the QCM substrate covered by the unannealed monolayer was 11 Hz. This frequency change is consistent with the loss of the 4-methoxyphenylisocyanide ligand ($\text{MeOC}_6\text{H}_4\text{N}\equiv\text{C}$), with a molar mass of 133 amu (Eq. 1).

A comparison of the UV-vis and XPS spectra of the films before and after annealing (see SI) reveals that after the annealing process the molecular structure remains unchanged and no flipping or profound rearrangement of the remaining organic molecular structure occurs. For instance, the UV-vis spectra of the pristine and annealed films of **2** show a similar profile, with the annealing films exhibit a peak at 273 nm characteristic of $\text{R}-\text{C}_6\text{H}_4-\text{C}\equiv\text{C}-\text{C}_6\text{H}_4-\text{R}'$

derivatives assembled in LB films.^[32] On the other hand, the amine peak in the XPS spectrum of pristine films of **2** appears at 399.9 eV, characteristic of amine groups being adsorbed onto the substrate surface. This peak remains unchanged after annealing which indicates that no flipping of the molecules occurs. A similar phenomenon has been observed for pristine and annealed LB films of **1**, where the carboxylic group remains adsorbed on the substrate surface after annealing (for more details see SI).

Thermal annealing of monomolecular LB films of **1** and **2** caused significant modification to the appearance, physical characteristics and composition of the film surface. For instance, **Figure 2** shows the AFM images of a pristine and an annealed **2** monolayer onto a flat mica substrate. The increase in the root mean square (RMS) roughness of the film (from 0.20 to 0.89 nm over areas of 9 μm^2) together with the appearance of bright spots distributed all over the film after the annealing process also indicates the presence of GNIs. In addition, a bearing analysis of the AFM image of the annealed LB film was performed in order to estimate the GNIs surface coverage. In a bearing analysis, the depths of all pixels of the image with respect to a reference point, i.e., the highest pixel are analyzed. This kind of analysis renders the estimation of the surface coverage and the estimation of depths. Thus, taking into account the volume of a gold atom and the bearing volume obtained from **Figure 2** (corrected by the tip convolution), a surface coverage of $7.2 \cdot 10^{-10}$ moles of gold atoms $\cdot\text{cm}^{-1}$ were obtained, which is in good agreement with the initial amount of gold in the pristine films ($7.5 \cdot 10^{-10}$ moles of gold atoms $\cdot\text{cm}^{-1}$). After annealing no mica bare regions are observed which is also in good agreement with the UV-vis and XPS results detailed above, and further supports that no reorganization of the underlying organic monolayer takes place upon annealing. As mentioned before, the chemical process behind these observations is the rupture of the P-Au-C or C-Au-C bonds and reduction of Au(I) to Au(0). After formation of Au(0) atoms, these gold atoms must diffuse on the surface to form the observed GNIs. In addition, since these GNIs are not protected by ligands they might be diffuse on the surface to form larger domains,

which is a phenomenon that could be very much influenced by temperature. To verify this point, monolayers of **2** were annealing for 2, 4, and 14 hrs and AFM images of these annealed films were obtained. These images (see SI) evidence diffusion of the GNIs to form larger clusters with increasing annealing times resulting in large areas not covered by GNIs.

Contact angle measurements are sensitive indicators of the surface properties of a monolayer.^[33-35] In this work, surface modification of monolayers after annealing is further evidenced by differences in water contact angle measurements from pristine and annealed films of **2** (by way of example) on glass. The contact angle of water on a pristine LB film of **2** is 67°, consistent with a well-formed hydrophobic LB film. After annealing at 100 °C for 2 h, followed by the rinsing and drying processes, the contact angle is reduced to 42° indicating a more hydrophilic surface. This contact angle is surprisingly close to the value associated with a bare gold substrate (39°).

One important question concerning the reliability of the TIDOC method for the production of GNIs decorated molecular films as nascent device structures has also been addressed: does diffusion and penetration of gold through the film cause short-circuits between the particle and underlying substrate? To answer this question the electrical properties of the junction-like structures were determined. For this purpose, *I-V* curves were recorded with a conductive-AFM (Bruker ICON) using the Peak Force Tunneling AFM (PF-TUNA™) mode as described before for other metal|organic monolayer|metal devices.^[15] The PF-TUNA™ operation mode for the AFM was chosen, instead of a STM or c-AFM in conventional contact mode, because it permits conductivity mapping of soft or fragile samples since the normal force is accurately controlled and lateral forces are avoided. This AFM mode is based in combining high frequency intermittent contact mode (several kHz) with AFM probes of low elastic constant and high resonance frequency (peak force tapping (™) mode). In this way, during the acquisition of images the damage suffered by tip and sample due to interaction forces is drastically reduced. This is important to precisely position the AFM tip on top of the GNI

before performing the current measurements. *I-V* curves on the metal|organic monolayer|GNI junctions are recorded using metal coated probes and a low-noise current amplifier. The *I-V* measurements are performed by positioning the AFM tip on top on the particle using Peak-Force Tapping, then the scanning is stopped, a contact is made between the tip and surface at the selected repulsive force, and the tip-sample voltage is swept while recording the electrical current. A compromise has to be made in order to select the most suitable contact force to be applied during the measurement since too much force will result in unacceptably large deformation of the monolayer underlying the GNIs, while too little force will result in inadequate electrical probing. The deformation or damage of the monolayer as a function of tip loading force (set-point force) has been investigated and the data are presented in the upper inset to **Figure 3** (refer to the solid black lines and scale to the right showing the apparent GNI height).

Figure 3 (inset bottom left) shows an AFM image of a film recorded using a set-point force of 3.5 nN. Three gold nanoislands labelled as GNI1, GNI2, and GNI3 are clearly visible in this image. When set-point forces between 3.5 and 27 nN are applied, the section analysis shows practically constant heights of 5.5, 5.2 and 4.2 nm for GNI1, GNI2, and GNI3, respectively (inset **Figure 3** top left). This result indicates that in this set-point force range no deformation or damage of the monolayer is apparent. If the set-point force is increased up to 35 nN, the section analysis of the GNIs gives heights of 4.3, 2.6 and 2.2 nm for GNI1, GNI2 and GNI3 respectively, revealing that when this set-point force is applied there is a deformation of the monolayer, with the GNIs being pushed down into the relatively soft underlying monolayer. If the set-point is increased to 44 nN, the deformation of the monolayer increases since the section analysis shows heights of 3.8, 2.1 and 1.8 nm for GNI1, GNI2 and GNI3, respectively. Moreover, if the set-point force is adjusted to low values, e.g. to 8.5 nN, the section analysis of these GNIs shows heights of 5.3, 5.2 and 4.1 nm which indicates that the deformation

produced in the monolayer after a high set-point force (35 or 44 nN) is applied is reversible and induces no apparent damage of the organic layer.

Once the influence of the applied set-point force in the monolayer was studied, the *I-V* curves were recorded. To record these current-voltage curves, the c-AFM tip was located on the GNI and a bias between the sample and the tip was applied. When a set-point force below 3.5 nN was used no current was detected, inset **Figure 3** top left, whilst set-point forces between 3.5 and 27 nN the *I-V* curves show low ($< 4 \times 10^{-5} G_0$) conductance values. These results suggest that when low set-point forces are used to record the *I-V* curves the electrical contact between the tip and the GNI is poor. Therefore, a set-point force of 35 nN is required to make a reasonable contact between the tip and the GNI while avoiding damage or excessive deformation of the organic layer during the determination of the electrical properties. Thus, the *I-V* curves were recorded by sweeping the tip voltage (± 1.1 V), using this force set-point once the AFM probe was placed on top of GNIs and a bias between the substrate and the tip was applied with the LB-coated Au substrate held at ground. *I-V* curves made on different GNIs produced fundamentally four distinct families of curves (representative curves from each family are shown in the SI, and a representative example is illustrated in Figure 3). Inset bottom right to **Figure 3** shows the conductance histogram built by adding all the experimental data in the -0.45 to 0.45 V ohmic region for each of the 350 *I-V* curves obtained experimentally by placing the AFM tip on top of the GNIs applying a set-point force of 35 nN. In addition, all the curves measured exhibit the typical shape observed for metal-molecule-metal junctions, with a linear section only at relatively low bias voltages and increasing curve gradients at higher bias. Importantly, only curves with this behavior were observed, both over GNIs and on the organic monolayer not covered by GNIs (see SI), and no low resistance traces characteristic of metallic short circuits were obtained over a wide range of set-point forces which rules out the presence of short-circuits. In addition, AFM images of complete areas do not show any evidence for protruding features in the organic monolayer which could

be the tops of filaments or monolayer damage. The representative *I-V* curve shown in **Figure 3** and also other representative curves obtained for the different families of curves fit in good agreement with the Simmons model^[36] (see details in the SI) revealing that the mechanism of transport through these metal|organic monolayer|GNIs sandwich structures is non-resonant tunneling. The determination of the electrical characteristics of **1** annealed monolayers was done following the same procedure (see SI) and the results were also consistent with the formation of metal|molecule|GNIs junctions without evidences of short circuits. Therefore, the TIDOC method, or thermal induced decomposition of an organometallic compound, is an alternative route for the solution of the top-contact electrode problem without damaging the organic layer or altering/contaminating the interfaces.

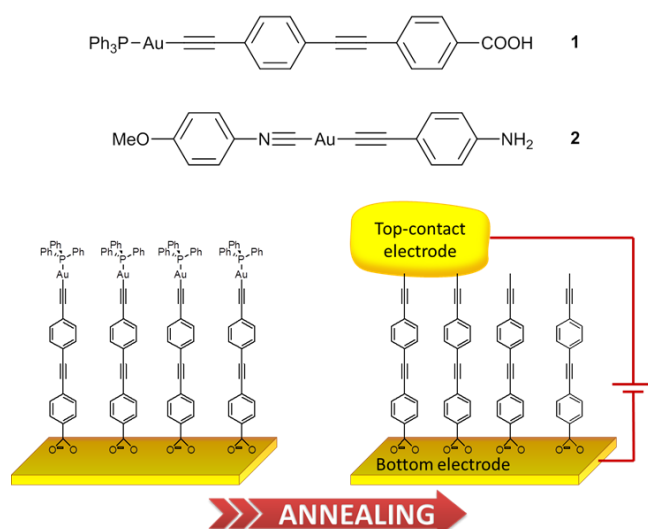
In conclusion, metal organic compounds, **1** and **2**, containing a gold atom in their structure have been synthesized and assembled into well-packed monomolecular films by means of the LB technique. Annealing of monomolecular films leads to the rupture of P-Au-C and C-Au-C bonds. Subsequent rinsing with chloroform eliminated the triphenylphosphine or isocyanide groups leading to GNIs remaining on the film surface as demonstrated by QCM, XPS (in the case of **1**) and AFM imaging. *I-V* curves collected from these metal|organic monolayer|GNIs sandwich structures are typical of metal-molecule-metal junctions, with no low resistance traces characteristic of metallic short circuits observed over a wide range of set-point forces. Therefore, the TIDOC method has shown itself as a clean, easy, cheap, and efficient procedure for the fabrication of top contact electrodes that minimizes the appearance of short-circuits which is a rather common problem in other traditional methods for the metallization of monolayers. These GNIs can be used at a later date as seeds for deposition of a thicker, more uniform metal top contact electrode using other methods such as electroless deposition, and work towards this goal is presently underway in our laboratories

Supporting Information

Supporting Information is available from the Wiley Online Library or from the author.

- [1] D. K. Aswal, S. Lenfant, D. Guerin, J. V. Yakhmi, D. Vuillaume, *Anal. Chim. Acta* **2006**, 568, 84.
- [2] R. W. Keyes, *Proc. IEEE* **2001**, 89.
- [3] P. Lindner, T. Glinsner, T. Uhrmann, V. Dragoi, T. Plach, T. Matthias, E. Pabo, M. Wimplinger, *Ieee International Soi Conference* **2012**.
- [4] R. K. Cavin, P. Lugli, V. V. Zhirnov, *Proc. of the IEEE* **2012**, 1720.
- [5] A. Kranti, G. A. Armstrong, *Semicond. Sci. Technol.* **2006**, 21, 409.
- [6] H. Iwai, *Microelectron. Eng.* **2009**, 86, 1520.
- [7] D. Vuillaume, *C. R. Physique* **2008**, 9, 78-94.
- [8] L. A. Zotti, T. Kirchner, J. C. Cuevas, F. Pauli, T. Huhn, E. Scheer, A. Erbe, *Small* **2010**, 6, 1929.
- [9] W. Wang, A. Scott, N. Gergel-Hackett, C. A. Hacker, D. B. Janes, C. A. Richter, *Nano Lett.* **2008**, 8, 478.
- [10] Editorial, *Nat. Nanotechnol.* **2013**, 8, 377.
- [11] Editorial, *Nat. Nanotechnol.* **2013**, 8, 385.
- [12] M. Ratner, *Nat. Nanotechnol.* **2013**, 8, 378.
- [13] H. Haick, D. Cahen, *Progress in Surf. Sci.* **2008**, 83, 217.
- [14] D. Vuillaume, *Proc. IEEE* **2010**, 1.
- [15] S. Martin, G. Pera, L. M. Ballesteros, A. J. Hope, S. Marqués-González, P. J. Low, F. Pérez-Murano, R. J. Nichols, P. Cea, *Chem. Eur. J.* **2014**, 20, 3421.
- [16] H. Haick, D. Cahen, *Accounts Chem. Res.* **2008**, 41, 359.
- [17] H. B. Akkerman, B. De Boer, *J. Phys.: Condens. Mater.* **2008**, 20, 013001.
- [18] R. L. McCreery, A. J. Bergren, *Adv. Mater.* **2009**, 21, 4303.
- [19] R. Chico, E. Castillejos, P. Serp, S. Coco, P. Espinet, *Inorg. CHem.* **2011**, 50, 8654.
- [20] L. M. Ballesteros, S. Martin, G. Pera, P. Schauer, K. Nicola, M. C. López, P. Low, R. J. Nichols, P. Cea, *Langmuir* **2011**, 7, 3600.

- [21] L. M. Ballesteros, S. Martín, C. Momblona, S. Marqués-González, M. C. López, R. J. Nichols, P. J. Low, P. Cea, *J. Phys. Chem. C* **2012**, *116*, 9142.
- [22] G. L. Gaines, *Insoluble monolayers at liquid-gas interface*, Interscience. John Wiley & Sons, New York, **1966**.
- [23] G. Sauerbrey, *Z. Physik* **1959**, *155*, 206ff.
- [24] H.-G. Boyen, G. Kästle, F. Weigl, B. Koslowski, C. Dietrich, P. Ziemann, J. P. Spatz, S. Riethmüller, C. Hartmann, M. Möller, G. Schmid, M. G. Garnier, P. Oelhafen, *Science* **2002**, *297*, 1533.
- [25] C. Shan, H. Yang, D. Han, Q. Zhang, A. Ivaska, L. Niu, *Biosens. Bioelectron* **2010**, *25*, 1070.
- [26] G. Liu, E. Luais, J. J. Gooding, *Langmuir* **2011**, *27*, 4176.
- [27] M. C. Bourg, A. Badía, R. B. Lennox, *J. Phys. Chem. B* **2000**, *104*, 6562.
- [28] I. Fratoddi, I. Venditti, C. Battocchio, G. Polzonetti, C. Cametti, M. V. Russo, *Nanoscale Res. Lett.* **2011**, *6*, 98.
- [29] C. G. Carson, R. A. Gerhardt, R. Tannenbaum, *J. Phys. Chem. B* **2007**, *111*, 14114.
- [30] M. J. Irwin, G. Jia, N. C. Payne, R. Puddephatt, *Organometallics* **1996**, *15*, 51.
- [31] M. A. Ansell, E. B. Cogan, C. J. Page, *Langmuir* **2000**, *16*, 1172.
- [32] G. Pera, A. Villares, M. C. López, P. Cea, D. P. Lydon, P. J. Low, *Chem. Mater.* **2007**, *19*, 857.
- [33] R. Maoz, J. Sagiv, *J. Coll. Interf. Sci.* **1984**, *100*, 465.
- [34] J. Gun, J. Sagiv, *J. Colloid Interface Sci.* **1986**, *112*, 457.
- [35] D. L. Allara, R. G. Nuzzo, *Langmuir* **1985**, *1*, 45.
- [36] J. G. Simmons, *J. Appl. Phys.* **1963**, *281*, 1793.



Scheme I. Top: [[4-{(4-carboxy)ethynyl}phenyl]ethynyl]-(triphenylphosphine)-gold, **1**, and [1-isocyano-4-methoxybenzene]-[4-amino-phenylethynyl]-gold, **2**. Bottom: cartoon showing the TIDOC method in which rupture of P-Au bonds after annealing of immobilized monolayers of **1** occurs leading to the formation of GNIs on the film surface. The triphenylphosphine group is eliminated by thoroughly rinsing the nanoisland decorated film with chloroform. The tolane group remains attached to the gold substrate by chemisorption of the acid group.

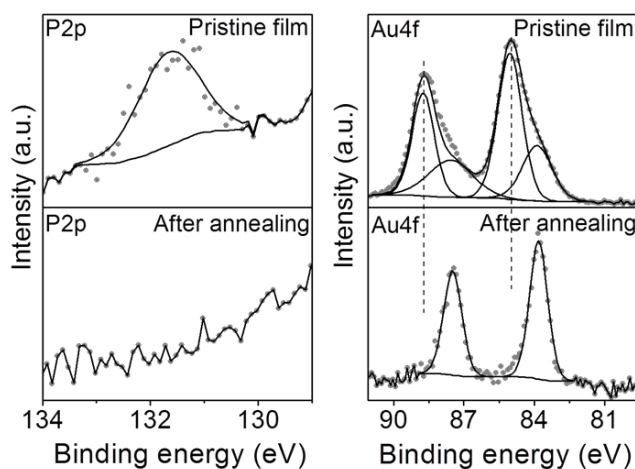


Figure 1. XPS spectra of P2p and Au4f photoelectrons of a **1** pristine monomolecular film transferred at $10 \text{ mN}\cdot\text{m}^{-1}$ onto a glass substrate and after annealing at $150 \text{ }^\circ\text{C}$ for 2 hours.

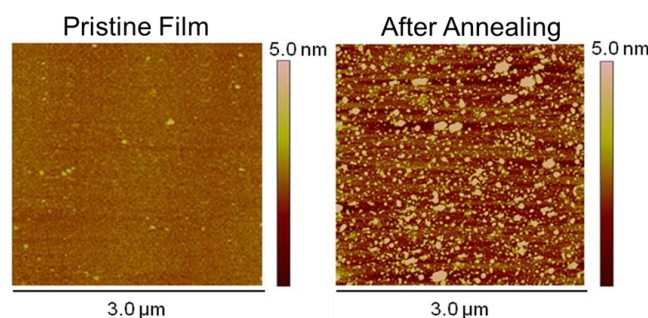


Figure 2. AFM images of a 2 pristine film onto a mica substrate and the same film after annealing.

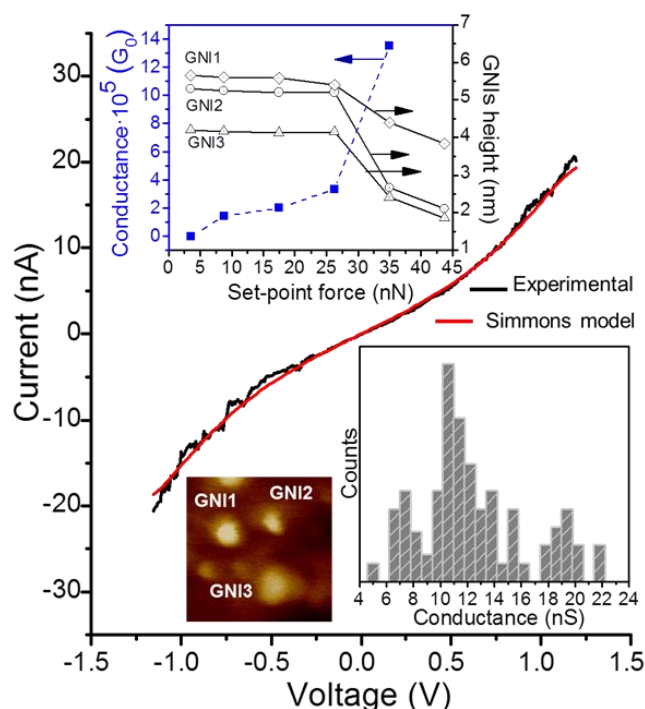


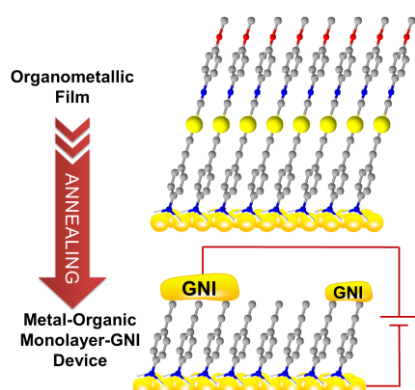
Figure 3. Representative I - V curve experimentally obtained by positioning the c -AFM tip on top of a GNI when a set-point force of 35 nN was applied (black line) and fitting according to the Simmons equation, $\Phi=0.69$ eV, $\alpha=0.78$ (red line); for further details see SI. Inset top left: height of GNIs determined with the c -AFM at the indicated set-point forces together with the average conductance values measured locating the tip of the c -AFM on the indicated GNIs. Inset bottom left: representative example of a 200×200 nm² image where GNIs can be clearly distinguished. These types of images were used to position the c -AFM tip onto the GNIs. Inset bottom right: conductance histogram built by adding all the experimental data from -0.45 to 0.45 V for each I - V curve obtained (ca. 350 curves).

The novel method for practical uses in the fabrication of the top contact electrode in a metal|organic monolayer|metal device involves the thermally induced decomposition of an organometallic compound, abbreviated as the TIDOC method. Monolayers incorporating the metal organic compounds (MOCs) were annealed at moderate temperatures, resulting in cleavage of the Au-P or Au-C bond and reduction of Au(I) to Au(0) as metallic gold nanoislands (GNIs).

Keyword:

Langmuir-Blodgett films; top-contact electrode; molecular junction

From an organometallic monolayer to an organic monolayer covered by metal nanoislands: a simple thermal protocol for the fabrication of the top contact electrode in molecular electronic devices



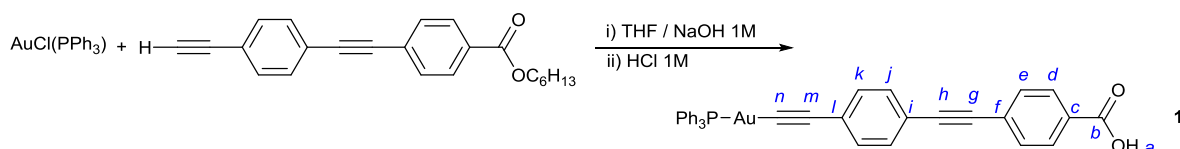
Supporting Information

From an organometallic monolayer to an organic monolayer covered by metal nanoislands: a simple thermal protocol for the fabrication of the top contact electrode in molecular electronic devices

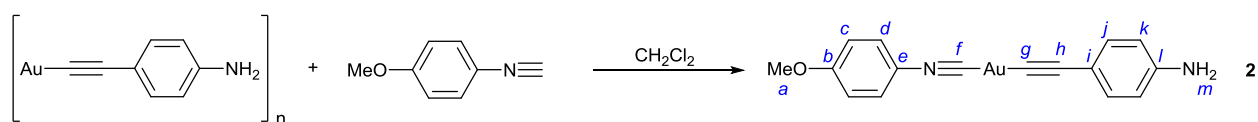
Luz Marina Ballesteros, Santiago Martín, Javier Cortés, Santiago Marqués-González, Francesc Pérez-Murano, Richard J. Nichols, Paul J. Low, and Pilar Cea*

1. Synthesis

General Conditions All reactions were carried out in oven-dried glassware under an oxygen-free nitrogen atmosphere using standard Schlenk techniques. The precursors hexyl 4-((4-ethynylphenyl)ethynyl)benzoate^[1] and AuCl(PPh₃)^[2] were prepared following literature procedures. The polymer [AuC≡CC₆H₄NH₂-4]_n^[3] was obtained by reaction of 4-ethynylaniline^[4] with AuCl(tht).^[5] Other reagents were purchased commercially and used as received. NMR spectra were recorded of the appropriate deuterated solvent solutions on a Varian VNMRS-600 spectrometer and referenced against solvent resonances. Infrared spectra were recorded on a Thermo 6700 spectrometer as Nujol mulls suspended between KBr plates. ESI mass spectra were recorded using a TQD mass spectrometer (Waters Ltd, UK) from 1 mg/mL in analytical grade methanol solutions. ASAP mass spectra were recorded from solid aliquots on an LCT Premier XE mass spectrometer (Waters Ltd, UK) or Xevo QToF mass spectrometer (Waters Ltd, UK) in which the aliquot is vaporized using hot N₂, ionized by a corona discharge and carried to the TOF detector (working range 100-1000 m/z). Microanalyses were carried out at the Science Centre, London metropolitan University.



Preparation of 1. In a 25 mL round bottom flask, chloro(triphenylphosphine)gold (I) (0.102 g, 0.206 mmol) and hexyl 4-((4-ethynylphenyl)ethynyl)benzoate (0.069 g, 0.209 mmol) were dissolved in THF (10 mL). To that solution, NaOH (1M, 5 mL) was added. The mixture was allowed to stir overnight at room temperature. The organic solvent was removed under vacuum and the remaining aqueous solution was acidified to pH ~2 by addition of HCl (1M). The off-white precipitate was isolated by centrifugation, washed with water (10 mL) and acetone (10 mL), and dried under vacuum. Yield 0.098 g, 0.139 mmol, 67.5 %. ^1H NMR (600 MHz, DMSO- d_6) δ 13.17 (*br. s*, 1H, *a*), 7.95 (d, $J = 8$ Hz, 2H, *d*), 7.62 (d, $J = 8$ Hz, 2H, *e*), 7.63-7.51 (m, 15H, *PPh*₃), 7.48 (d, $J = 8$ Hz, 2H, *k/j*), 7.37 (d, $J = 8$ Hz, 2H, *k/j*). $^{13}\text{C}\{^1\text{H}\}$ NMR (151 MHz, DMSO- d_6) δ 167.12 (*b*), 134.35 (d, $J = 14$ Hz, *PPh*₃), 132.43 (*br*, *PPh*₃), 132.12 (*k/j*), 132.02 (*k/j*), 131.92 (*e*), 131.06 (*c/f/g*), 130.08 (d, $J = 11$ Hz, *PPh*₃), 130.00 (*d*), 129.62 (d, $J = 56$ Hz, *PPh*₃), 126.98 (*c/f/g*), 126.46, 120.20, 102.98, 92.39 (*m/l/i/h*), 90.30 (*c/f/g*), (*n*, not observed). $^{31}\text{P}\{^1\text{H}\}$ NMR (243 MHz, DMSO- d_6) δ 41.5 (s, *PPh*₃). IR (*nujol*): 3391 cm^{-1} (*br*) $\nu(\text{COOH})$, 2216, 2108 cm^{-1} (*w*) $\nu(\text{C}\equiv\text{C})$, 1682 cm^{-1} (*s*) $\nu(\text{C}=\text{O})$. MS⁺ (ASAP) (*m/z*) 705.1 (4, $[\text{M}+\text{H}]^+$), 263.1 (100, $[\text{M}-\text{AuPPh}_3+\text{O}]^+$).



Preparation of 2. To a suspension of $[\text{AuC}\equiv\text{CC}_6\text{H}_4\text{NH}_2-4]_n$ (0.051 g, 0.16 mmol), in CH_2Cl_2 (10 mL) 4-methoxyphenyl isocyanide (0.024 g, 0.18 mmol) was added. The mixture was stirred at room temperature for 30 minutes. Upon complete dissolution, the mixture was concentrated by solvent evaporation (~2 mL) and the desired product was precipitated upon addition of hexane. The light-brown powder was collected by filtration, washed thoroughly with hexane and ether (2 mL) and dried in air (0.049 g, 0.11 mmol, 69 %). ^1H NMR (600 MHz, CDCl_3) δ 7.45 (d, $J = 9$ Hz, 2H, *d*), 7.29 (d, $J = 9$ Hz, 2H, *k*), 6.94 (d, $J = 9$ Hz, 2H, *c*), 6.56 (d, $J = 9$ Hz, 2H, *j*), 3.85 (s, 3H, *a*), 3.70 (s, 2H, *m*). $^{13}\text{C}\{^1\text{H}\}$ NMR (151 MHz, CDCl_3) δ

161.52 (*b*), 145.50 (*g/h/i/l*), 133.73 (*k*), 128.48 (*d*), 119.03 (*g/h/i/l*), 116.91 (*e*), 115.19 (*c*), 114.58 (*j*), 114.21 (*g/h/i/l*), 104.52 (*g/h/i/l*), 55.78 (*a*), (*f*, not observed). IR (*nujol*): 3439, 3354 cm^{-1} (*m*) $\nu(\text{NH}_2)$, 2214 cm^{-1} (*s*) $\nu(\text{N}\equiv\text{C})$, 2210 cm^{-1} (*w*) $\nu(\text{C}\equiv\text{C})$. MS (ESI)⁺ (*m/z*) 447.6 (100, $[\text{M}+\text{H}]^+$). Elemental analysis % calcd. (found): C 43.06 (42.92); H 2.94 (2.94); N 6.28 (6.39).

2. Experimental Section

The films of 1 and 2 were prepared on a Nima Teflon trough with dimensions (720x100) mm^2 , which was housed in a constant temperature (20 ± 1 °C) clean room. A Wilhelmy paper plate pressure sensor was used to measure the surface pressure (π) of the monolayers. The sub-phase was Millipore Milli-Q water, resistivity 18.2 $\text{M}\Omega\cdot\text{cm}$. A solution of the MOC 1 or 2 in chloroform (LabScan HPLC grade 99.8%) was delivered from a Hamilton syringe held very close to the surface, allowing the surface pressure to return to a value as close as possible to zero between each addition. The spreading solvent was allowed to completely evaporate from the surface of the sub-phase over a period of at least 20 min before compression of the monolayer commenced at a constant sweeping speed of $0.015 \text{ nm}^2\cdot\text{molecule}^{-1}\cdot\text{min}^{-1}$. The direct visualization of the monolayer formation at the air/water interface was studied using a commercial micro-Brewster angle microscopy (micro-BAM) from KSV-NIMA, having a lateral resolution better than 12 μm .

The solid substrates used for the transferences were cleaned carefully as described elsewhere.^[6-7] The monolayers were deposited onto glass, mica, quartz, and gold substrates at a constant surface pressure by the vertical dipping method (dipping speed 3 $\text{mm}\cdot\text{min}^{-1}$). Quartz Crystal Microbalance (QCM) measurements were carried out using a Stanford Research System instrument, with a frequency counter with 0.1 Hz resolution, and employing AT-cut, α -quartz crystals with a resonant frequency of 5 MHz having circular gold electrodes patterned on both sides. Atomic Force Microscopy (AFM) experiments were performed by

means of a Multimode 8 AFM system from Veeco, using the tapping mode. The data were collected with a silicon cantilever provided by Bruker, with a force constant of $40 \text{ mN}\cdot\text{m}^{-1}$ and operating at a resonant frequency of 300 kHz. The images were collected with a scan rate of 1 Hz, an amplitude set point lower than 1 V, and in ambient air conditions. UV-vis spectra of the LB films were acquired on a Varian Cary 50 spectrophotometer, and recorded using a normal incident angle with respect to the film plane. Contact angle experiments were performed with a commercial optical tensiometer Theta Lite from Attension.

X-ray photoelectron spectroscopy (XPS) spectra were acquired on a Kratos AXIS ultra DLD spectrometer with a monochromatic Al $K\alpha$ X-ray source (1486.6 eV) using a pass energy of 20 eV. The photoelectron take-off angle was 90° with respect to the sample plane. To provide a precise energy calibration, the XPS binding energies were referenced to the C(1s) peak at 284.6 eV.

All the conducting-AFM (c-AFM) measurements were performed with a Bruker ICON microscope under humidity control, ca. 30%, with a N_2 flow, using the Peak Force Tunneling AFM (PF-TUNATM) mode, and employing a PF-TUNATM cantilever from Bruker (coated with Pt/Ir 20 nm, ca. 25 nm radius, $0.4 \text{ N}\cdot\text{m}^{-1}$ spring constant and 70 kHz resonance frequency).

The films of 1 and 2 were prepared on a Nima Teflon trough with dimensions (720x100) mm^2 , which was housed in a constant temperature ($20\pm 1^\circ\text{C}$) clean room. A Wilhelmy paper plate pressure sensor was used to measure the surface pressure (π) of the monolayers. The sub-phase was Millipore Milli-Q water, resistivity $18.2 \text{ M}\Omega\cdot\text{cm}$. A solution of the MOC 1 or 2 in chloroform (LabScan HPLC grade 99.8%) was delivered from a Hamilton syringe held very close to the surface, allowing the surface pressure to return to a value as close as possible to zero between each addition. The spreading solvent was allowed to completely evaporate from the surface of the sub-phase over a period of at least 20 min before compression of the

monolayer commenced at a constant sweeping speed of $0.015 \text{ nm}^2 \cdot \text{molecule}^{-1} \cdot \text{min}^{-1}$. The direct visualization of the monolayer formation at the air/water interface was studied using a commercial micro-Brewster angle microscopy (micro-BAM) from KSV-NIMA, having a lateral resolution better than $12 \text{ }\mu\text{m}$.

The solid substrates used for the transferences were cleaned carefully as described elsewhere.^[6-7] The monolayers were deposited onto glass, mica, and gold substrates at a constant surface pressure by the vertical dipping method (dipping speed $3 \text{ mm} \cdot \text{min}^{-1}$). Quartz Crystal Microbalance (QCM) measurements were carried out using a Stanford Research System instrument and employing AT-cut, α -quartz crystals with a resonant frequency of 5 MHz having circular gold electrodes patterned on both sides. Atomic Force Microscopy (AFM) experiments were performed by means of a Multimode 8 AFM system from Veeco, using the tapping mode. The data were collected with a silicon cantilever provided by Bruker, with a force constant of $40 \text{ mN} \cdot \text{m}^{-1}$ and operating at a resonant frequency of 300 kHz. The images were collected with a scan rate of 1 Hz, an amplitude set point lower than 1 V, and in ambient air conditions. Contact angle experiments were performed with a commercial optical tensiometer Theta Lite from Attension.

X-ray photoelectron spectroscopy (XPS) spectra were acquired on a Kratos AXIS ultra DLD spectrometer with a monochromatic Al $K\alpha$ X-ray source (1486.6 eV) using a pass energy of 20 eV. The photoelectron take-off angle was 90° with respect to the sample plane. To provide a precise energy calibration, the XPS binding energies were referenced to the C(1s) peak at 284.6 eV.

All the conducting-AFM (c-AFM) measurements were performed with a Bruker ICON microscope under humidity control, ca. 30%, with a N_2 flow, using the Peak Force Tunneling AFM (PF-TUNATM) mode, and employing a PF-TUNATM cantilever from Bruker (coated with Pt/Ir 20 nm, ca. 25 nm radius, $0.4 \text{ N} \cdot \text{m}^{-1}$ spring constant and 70 kHz resonance frequency).

Fabrication of Langmuir films of **1**. The protocol to fabricate true monolayers of **1** at the air-water interface was carefully designed and tested with the aim of decreasing the molecular forces among MOCs which may lead to the formation of three dimensional aggregates, due to the π - π , hydrogen bonds, and aurophilic^[8-10] intermolecular interactions as described in the previous section. Reproducible surface pressure vs. area per molecule, π - A , isotherms were obtained together with Brewster Angle Microscopy images that rule out the presence of three dimensional aggregates (Figure S1).

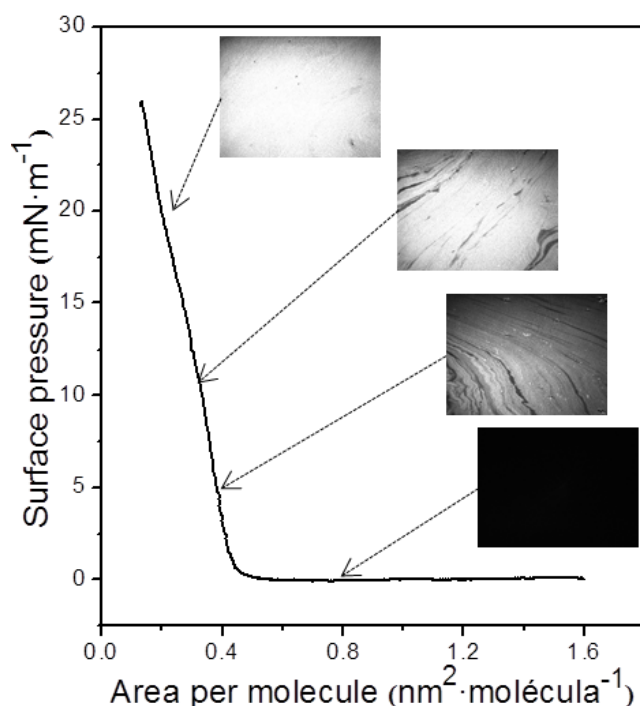


Figure S1. Surface pressure vs. area per molecule (π - A) of **1** at 20 °C, and BAM images of **1** at the air-liquid interface at the indicated surface pressures. The field of view along the x axes for the BAM images is 800 μm .

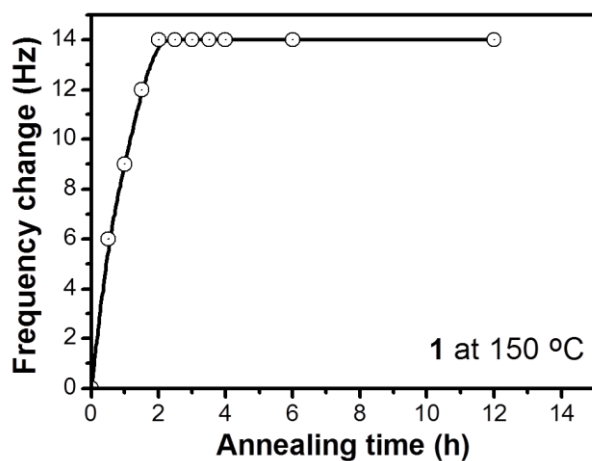
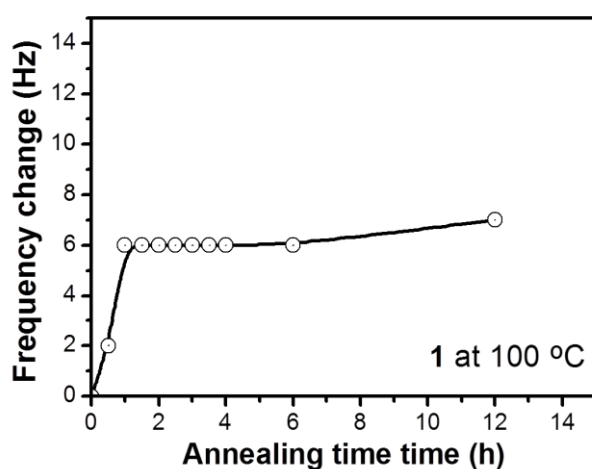
The deposition ratio, τ , was determined by two methods. First, from Equation S1:^[11]

$$\tau = S_1 / S_0 \quad (\text{S.1})$$

where S_0 is the geometrical surface of the solid substrate and S_1 represents the reduction of the surface occupied by the Langmuir film at the air-water interface due to the transference process. This equation yields a deposition ratio equal to 1. This transfer ratio was also determined by the variation in the resonance frequency of a quartz crystal substrate before and

after the deposition of a monomolecular film (Equation 1 in the paper), which also leads to a transfer ratio close to 1 and a surface coverage of $5.5 \cdot 10^{-10} \text{ mol} \cdot \text{cm}^{-2}$.

Optimization of the annealing conditions of LB films of 1. The optimum annealing conditions for the decomposition of LB films of **1** were studied with the QCM. Figure S2 shows the change in the frequency of a monomolecular LB film of **1** deposited onto a QCM substrate after annealing for the indicated times and the subsequent rinsing and drying processes.



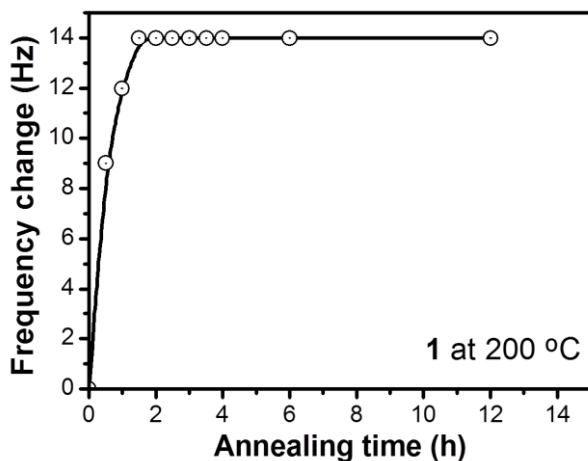


Figure S2. Frequency change upon the annealing time for a monomolecular LB film of **1** at the indicated temperatures.

Langmuir and Langmuir-Blodgett films of 2. Figure S3 shows a reproducible isotherm of **2** which is characterized by a zero surface pressure in the 2.2-0.4 nm²·molecule⁻¹ range, featuring a lift-off at ca. 0.4 nm²·molecule⁻¹ followed by a monotonous increase of the surface pressure upon compression.

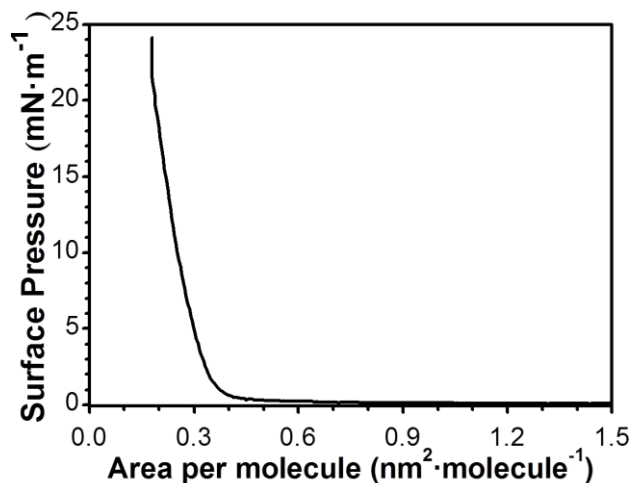
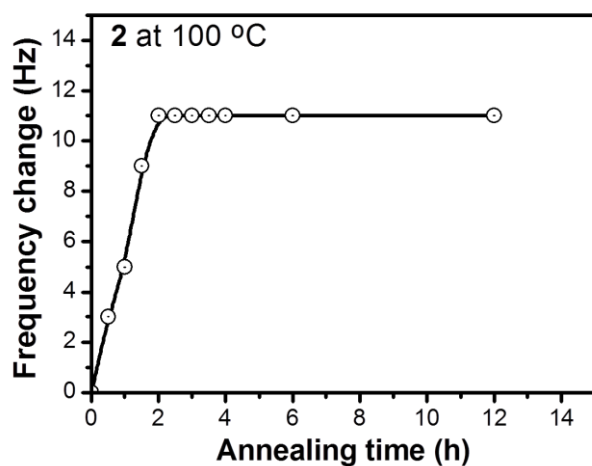
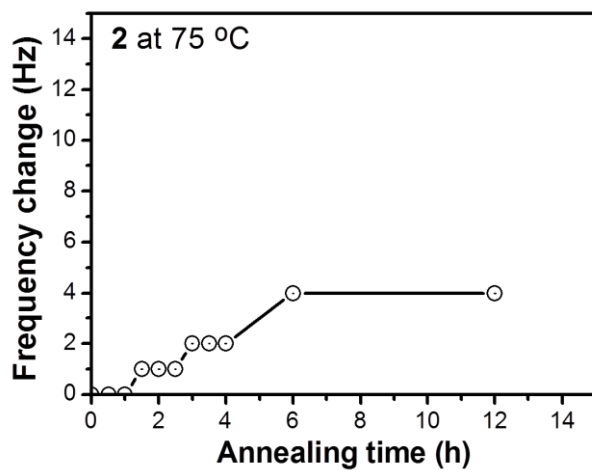


Figure S3. Surface pressure vs. area per molecule (π -A) recorded at 20 °C.

Langmuir monolayers were transferred onto solid substrates by the vertical dipping method onto mica, glass and gold substrates at several surface pressures of transference. During the upstroke process the deposition ratio is close to unity (~ 1) for a transference surface pressure of 16 mN·m⁻¹ (area per molecule of 0.21 nm²) calculated using Eq. S.1. This transfer ratio was also determined by the variation in the resonance frequency of a quartz crystal substrate before

and after the deposition of a monomolecular film (Equation 1 in the paper), which also leads to a transfer ratio close to 1 and a surface coverage of $7.5 \cdot 10^{-10} \text{ mol} \cdot \text{cm}^{-2}$. This value is in excellent agreement with molecular models which predict an area per molecule of $0.21 \text{ nm}^2 \cdot \text{molecule}^{-1}$ (Spartan[®] 08 V 1.0.0).

Optimization of the annealing conditions of 2



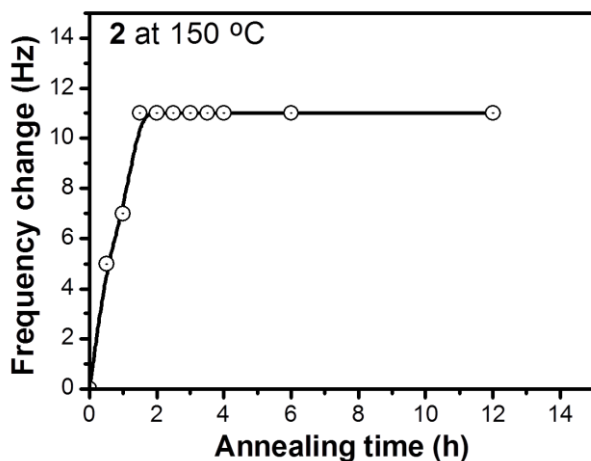


Figure S4. Frequency change upon the annealing time for a monomolecular LB film of **2** at the indicated temperatures.

XPS spectra of the C1s region for 1. Figure S5 shows the XPS spectra of **1** in powder, pristine and annealed LB films. The C1s region for the powder shows a peak at 288.6 eV attributable to the carboxylic acid group,^[12-14] while the pristine and the annealed LB films show a peak at 287.1 eV attributable to the carboxylate group.^[15-16] These results seem to indicate that after annealing the carboxylate group remains attached to the glass surface of the substrate.

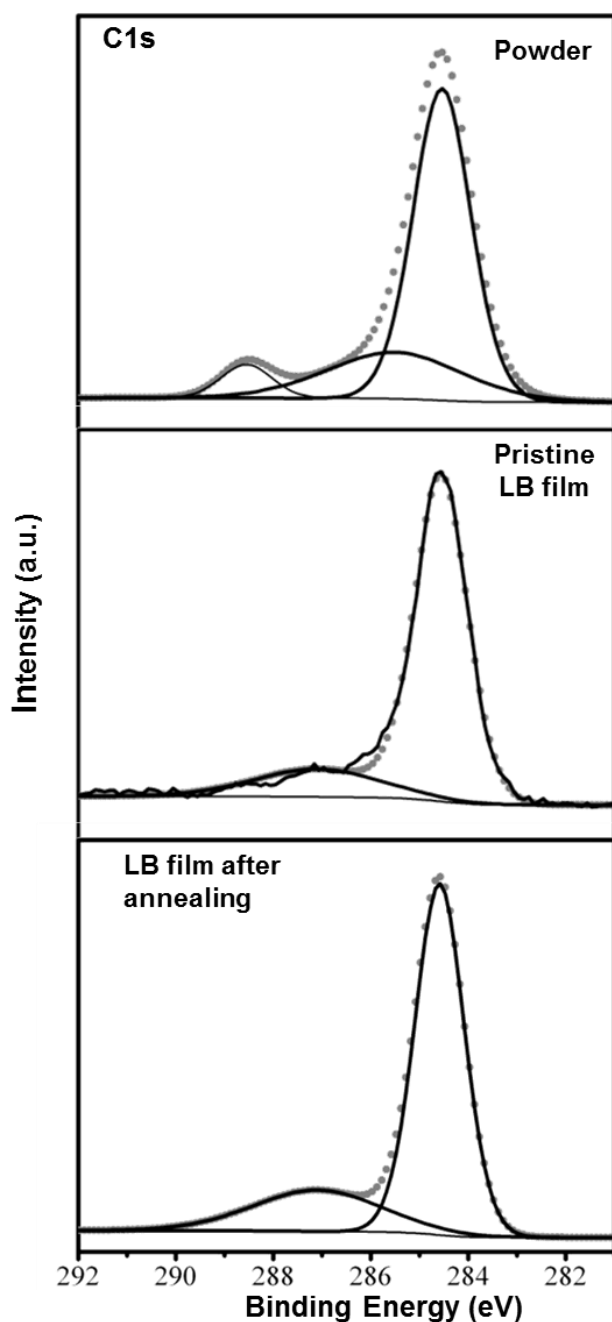


Figure S5. XPS spectra of C1s photoelectrons of **1** in powder, assembled in a pristine monomolecular film transferred at $10 \text{ mN}\cdot\text{m}^{-1}$ and after annealing at $150 \text{ }^\circ\text{C}$ for 2 hours.

XPS spectra of the Au4f region for 2. Figure S6 shows the XPS spectra of **2** in powder, pristine and annealed LB films. The Au4f region for the film after the annealing process shows two peaks at 84.1 and 87.8 eV, attributable to Au(0) ^[17-19] whilst the XPS-spectrum of the powder exhibits two intense peaks at 85.3 y 88.8 eV, attributable to Au4f_{5/2} and Au4f_{7/2} in Au(I).^[20-21] The spectrum of pristine **2** LB films also shows a doublet for the gold peak

practically in the same position as the powder spectrum, indicating that the reduction of gold only takes place after the annealing process.

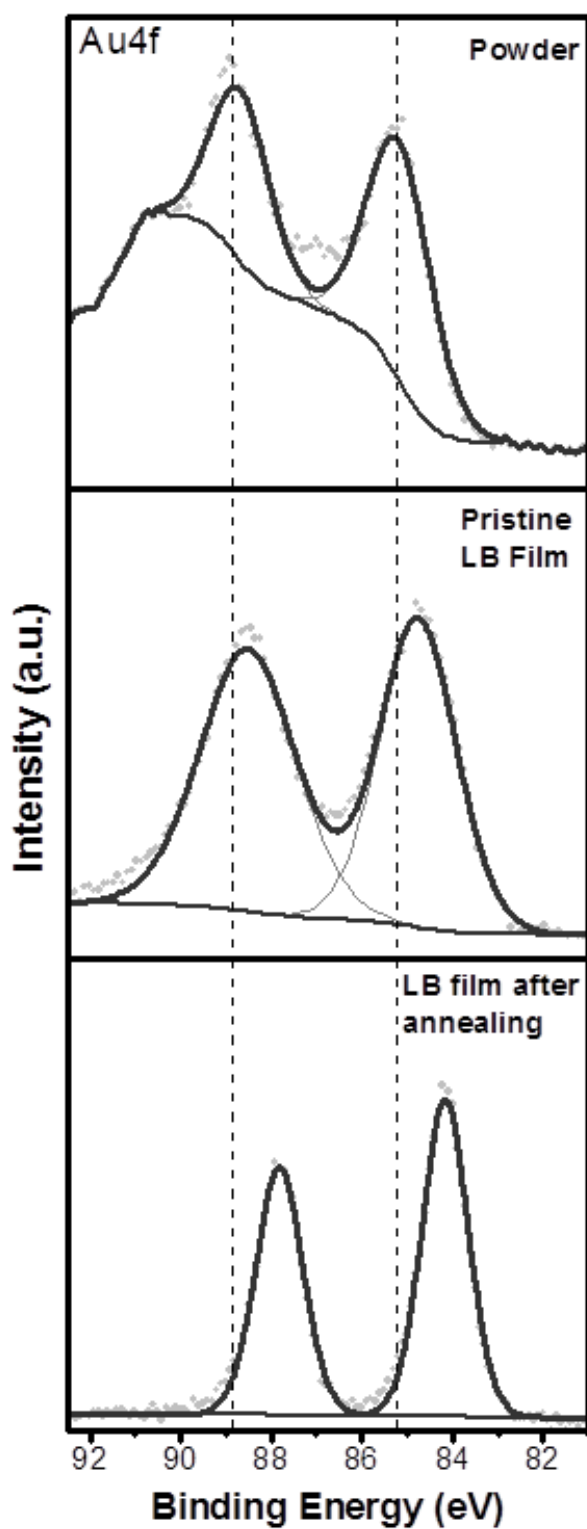


Figure S6. XPS spectra of Au4f photoelectrons of **2** in powder, assembled in a pristine monomolecular film transferred at $16 \text{ mN}\cdot\text{m}^{-1}$ and after annealing at $100 \text{ }^\circ\text{C}$ for 2 hours.

XPS spectra of the N1s region for 2.

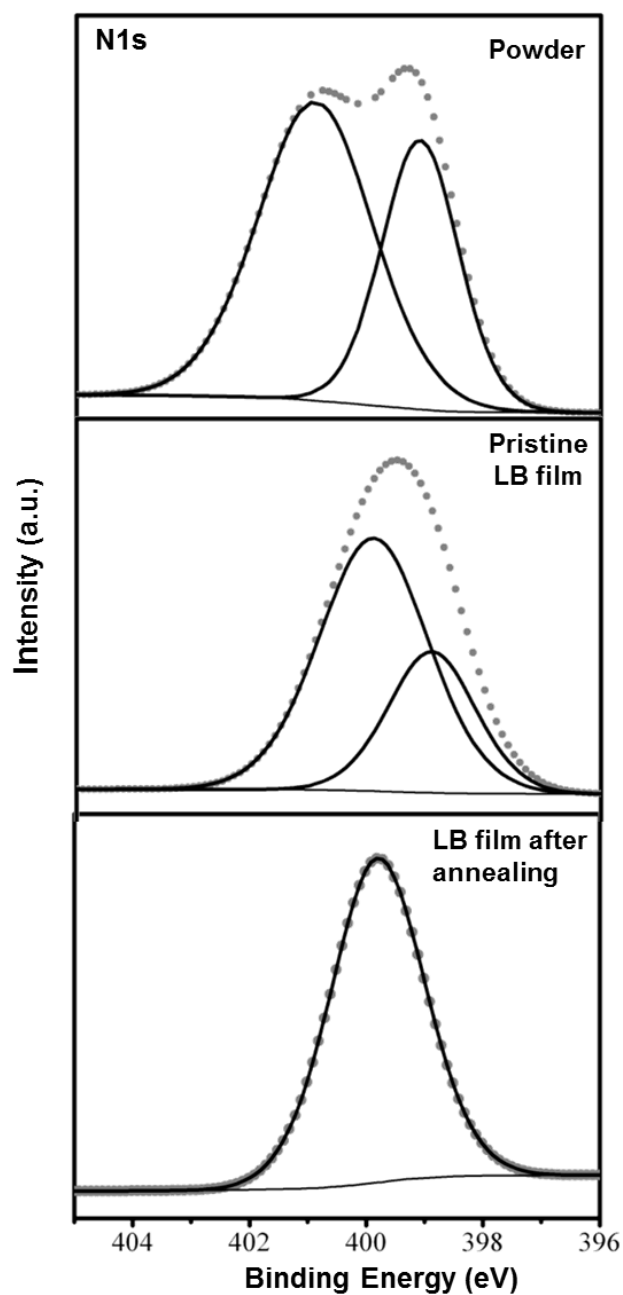


Figure S7. XPS spectra of N1s photoelectrons of **2** in powder, assembled in a pristine monomolecular film transferred at $16 \text{ mN}\cdot\text{m}^{-1}$ and after annealing at $100 \text{ }^\circ\text{C}$ for 2 hours.

UV-vis of pristine and annealed films of 2

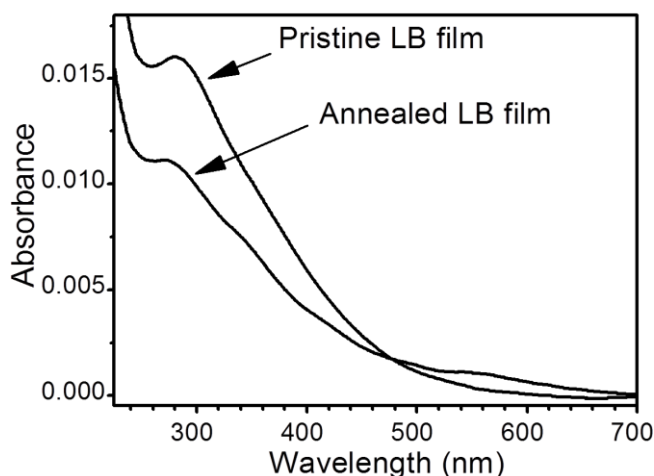


Figure S8. UV-vis spectra of pristine and annealed LB films of 2. The profile of the two spectra is similar with the annealing film exhibiting the characteristic tolane band and the gold plasmon band.

AFM images at several annealing times

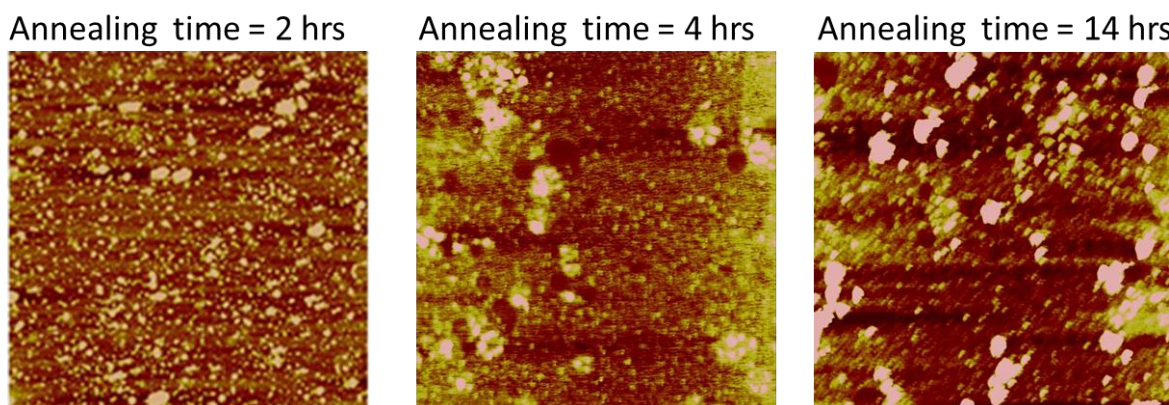


Figure S9. AFM images of 2 LB films recorded after the indicated annealing times. Both the diameter and height of the gold nanoislands increase upon increasing annealing times. The images are $3 \times 3 \mu\text{m}^2$ and 5 nm in height.

Conducting-AFM measurements for 1. A similar study to the one reported in the paper for compound 2 was also performed on annealed LB films of 1 to determine the electrical properties of the sandwiched metal|monolayer|GNIs structures fabricated for this compound. Inset of Figure S10 shows an AFM image of a LB film of 1 after annealing at 150 °C for 2 hours using a set-point force of 1.5 nN where three gold nanoislands labelled as GNI1, GNI2, and GNI3 are clearly visible. When the applied set-point force was in the 1.5 to 17 nN range,

the section analysis shows practically constant heights of 9.1, 8.9 and 7.5 nm for GNI1, GNI2, and GNI3, respectively revealing that in this set-point force range no deformation or damage of the monolayer occurs, Figure S10. Nevertheless, if the set-point force is between 17 and 43 nN a continuous deformation of the monolayer takes place since the section analysis shows heights of 9.0, 8.9 and 7.4 nm (at 17 nN) to 8.0, 7.7 and 6.2 nm (at 43nN) for GNI1, GNI2 and GNI3 respectively. If the set-point force is turned to low values, e.g. to 8.5 nN, the section analysis of these GNIs shows heights of 9.0, 8.8 and 7.3 nm which indicates that the deformation produced in the monolayer after applying a high set-point force (43 nN) is reversible and does not induce damage in the organic layer. After this study the *I-V* curves were recorded for all range of the set-point forces used. When a set-point force used was 1.5 or 3.5 nN no current was detected. Meanwhile for a set-point force between 3.5 and 17 nN the *I-V* curves show low conductance suggesting that when low set-point forces are used to record the *I-V* curves the contact between the tip and the GNI is poor. Nevertheless, when a set-point force of 26 nN is used to record the *I-V* curves, the curves show a significant conductance revealing that for this set-point force the contact between the tip and the GNI is good without damaging the monolayer.

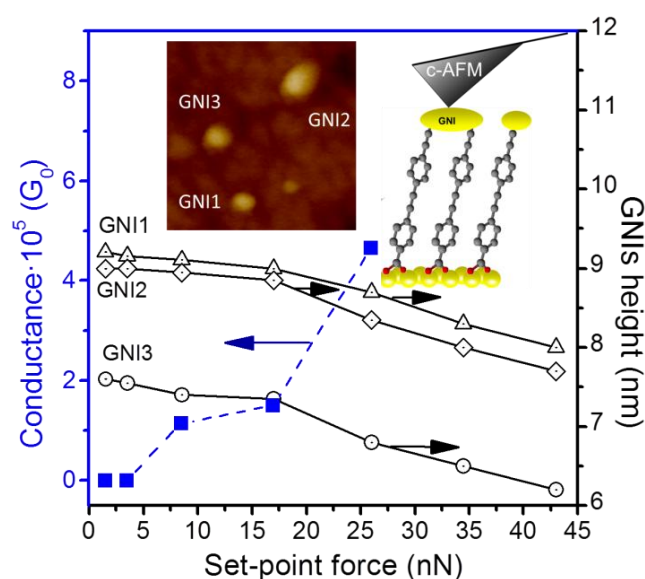


Figure S10. Height of GNIs determined with the c-AFM at the indicated set-point forces together with the average conductance values measured locating the tip of the c-AFM on the

indicated GNIs. The inset top left image shows a representative example of a 400 x 400 nm² image where GNIs can be clearly distinguished and was used to position the c-AFM tip onto the GNIs. The inset top right cartoon shows a scheme of the c-AFM tip in contact with a GNI for the measurement of the electrical properties of the sandwiched metal|monolayer|GNI structures.

Figure S11 shows representative I - V curves of the three distinct families of curves obtained for the metal|organic monolayer of 1|GNIs sandwich structures recorded when the c-AFM tip was positioned on top of the GNIs at a set-point force of 35 nN. A widely applied tunnelling model that can be used for comparison with the experimental I - V data is the Simmons model.^[22] In this model, the current I is given by:

$$I = \frac{Ae}{4\pi^2\hbar s^2} \left\{ \left(\Phi - \frac{eV}{2} \right) \exp \left[-\frac{2(2m)^{1/2}}{\hbar} \alpha \left(\Phi - \frac{eV}{2} \right)^{1/2} s \right] - \left(\Phi + \frac{eV}{2} \right) \exp \left[-\frac{2(2m)^{1/2}}{\hbar} \alpha \left(\Phi + \frac{eV}{2} \right)^{1/2} s \right] \right\} \quad (\text{S.2})$$

where V is the applied potential, A is the contact area (0.33 nm² according to the isotherm shown in Figure 1 at the surface pressure of transference, 10 mN·m⁻¹), s is the width of the tunnelling barrier which was assumed to be the distance between the end group (carboxylic acid) and the GNI (0.88 nm), Φ is the effective barrier height of the tunnelling junction (relative to the Fermi level of the Au), α is related to the effective mass of the tunnelling electron and m and e represent the mass and the charge of an electron, respectively. To fit the I - V data in Figure S11, Φ and α are the fit parameters. The curves shown in Figure S11 fit in good agreement with the Simmons model^[22] revealing that the mechanism of transport through these metal|organic monolayer of 1|GNI sandwich structures is also non-resonant tunneling.

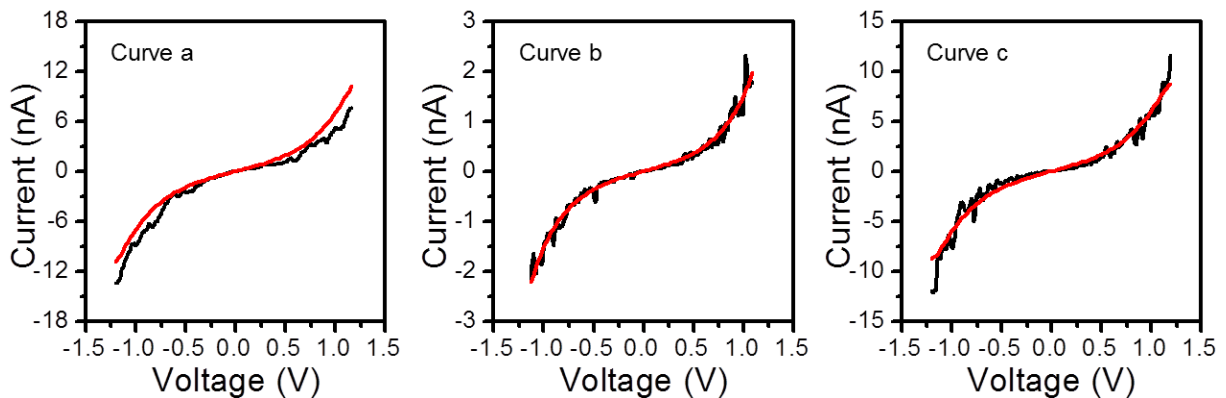


Figure S11. Representative I - V curves obtained by positioning the c-AFM tip on top of the GNIs when a set-point force of 35 nN was applied (black line) and fitting according to the Simmons equation (red line): (a) $\Phi=0.69$ eV, $\alpha=0.78$; (b) $\Phi=0.74$ eV, $\alpha=0.57$; and (c) $\Phi=0.66$ eV, $\alpha=0.65$.

A conductance histogram built by adding all the experimental data from -0.45 to 0.45 V (the ohmic region) for each I - V curve obtained (320 curves) reveals that the most representative I - V curve of all these curves is curve a, whose conductance correlates to the main peak of conductance in the histogram (Figure S12). As for **2**, all the measured curves both over GNIs and over the organic monolayer (places where there are not GNIs) show a shape commonly observed for metal-molecule-metal junctions, with a linear section only at relatively low bias voltages and increasing curve gradients at higher bias. In addition, only curves with this behavior were observed and no low resistance traces characteristic of metallic short circuits were obtained over a wide range of set-point forces which rule out the presence of short-circuits.

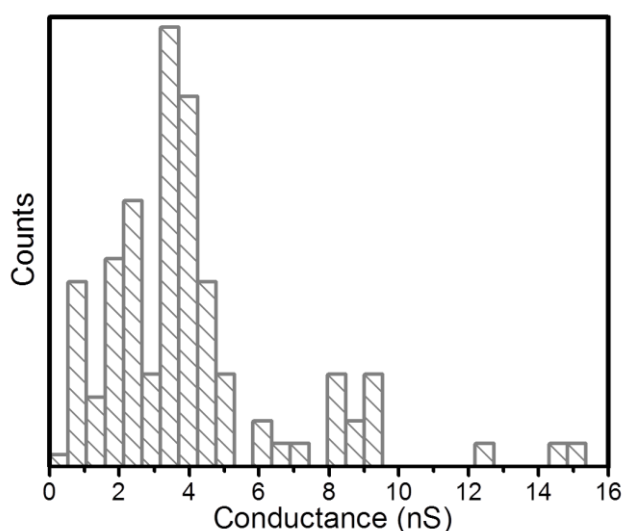


Figure S12. Conductance histogram built by adding all the experimental data from -0.45 to 0.45 V for each I - V curve obtained (ca. 320 curves).

Conducting-AFM measurements for **2.** All the representative I - V curves shown in Figure S13 for metal|monolayer|GNI junctions indicate that the mechanism of transport is non-resonant tunnelling. A good agreement between the data and the model is obtained with $\Phi =$

0.69 eV and $\alpha = 0.78$ for curve a; $\Phi=0.67$ eV and $\alpha=0.83$ for curve b; $\Phi=0.75$ eV and $\alpha=0.86$ for curve c; and $\Phi=0.64$ eV and $\alpha=0.69$ for curve d.

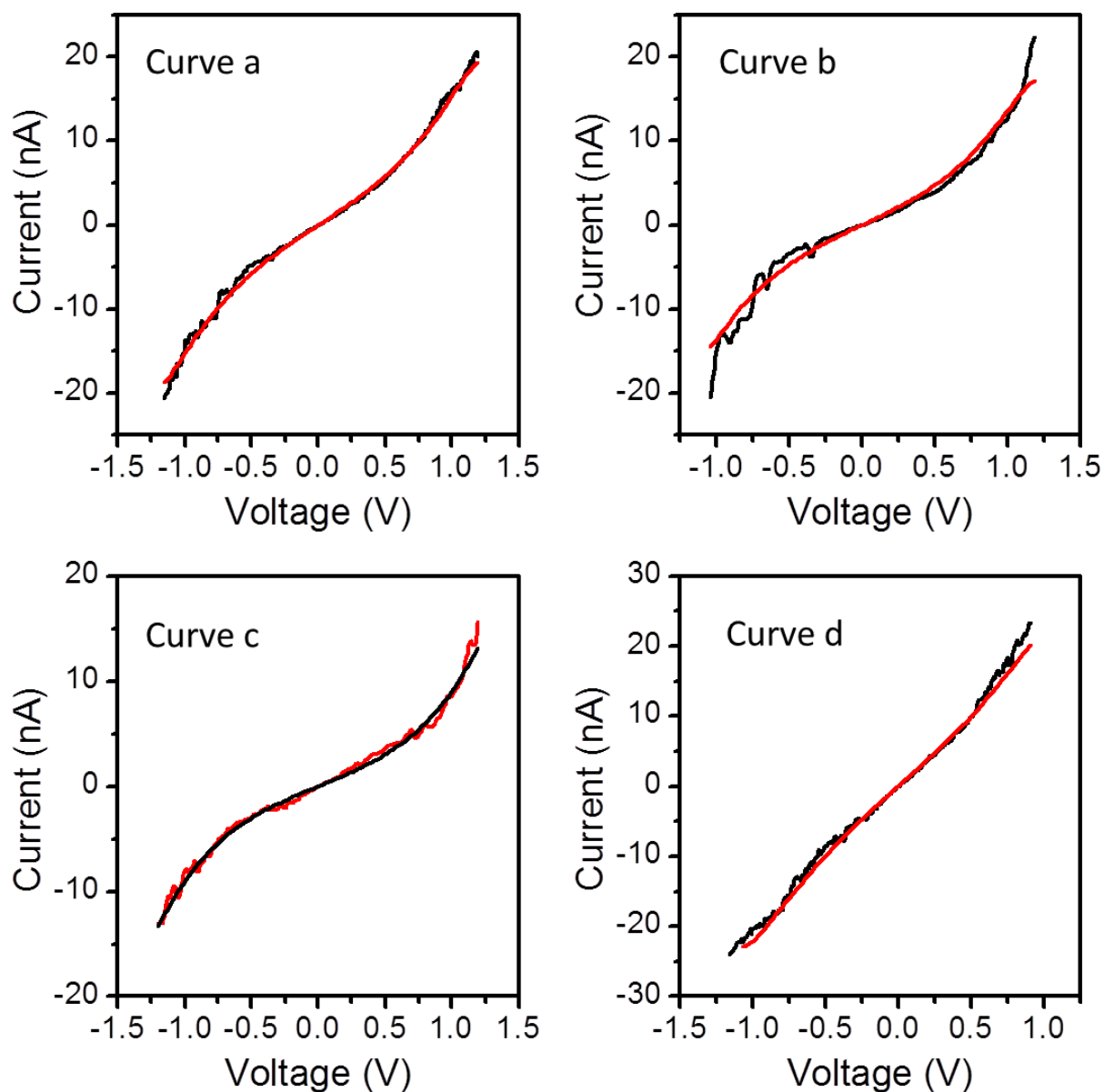


Figure S13. *I-V* curves obtained by positioning the c-AFM tip on top of the GNIs when a set-point force of 35 nN was applied. The four curves shown are representative of the distinct families obtained (black line) and fitting according to the Simmons equation (red line): (a) $\Phi=0.69$ eV, $\alpha=0.78$; (b) $\Phi=0.67$ eV, $\alpha=0.83$; (c) $\Phi=0.75$ eV, $\alpha=0.86$, (d) $\Phi=0.64$ eV, $\alpha=0.69$. A is 0.21 nm^2 according to the isotherm shown in Figure S3 at the surface pressure of transference, $16 \text{ mN}\cdot\text{m}^{-1}$, and, s , the width of the tunnelling barrier, was assumed to be the distance between the end group (amine) and the GNI, i.e. 1.66 nm.

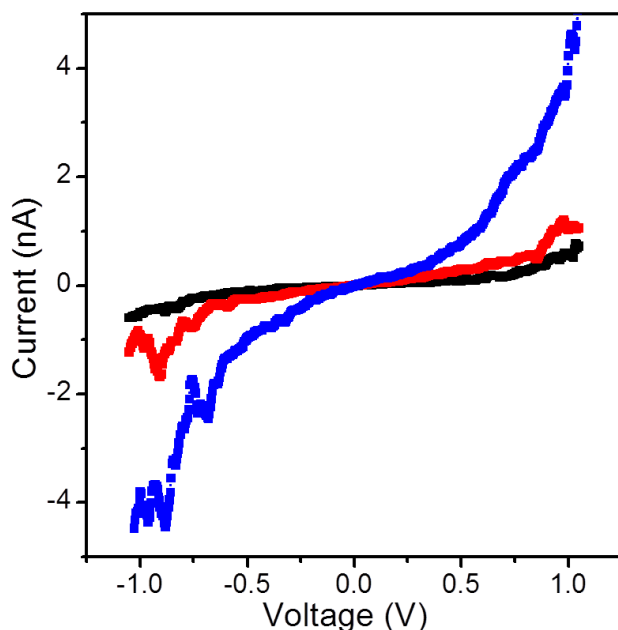


Figure S14. Representative I - V curves obtained by positioning the c-AFM tip onto a **2** monomolecular LB film deposited onto a gold substrate when a set-point force of 3.5 (black), 8.75 (red) and 17.5 nN (blue) was applied. The shape of these curves with a linear section only at relatively low bias voltages and increasing curve gradients at higher bias are characteristics of metal-molecule-metal junctions and rule out the presence of short-circuits. Damage on the LB film is produced when higher set-point forces are applied.

Acknowledgements

S.M. F.P.-M and P.C. are grateful for financial assistance from Ministerio de Economía y Competitividad from Spain and FEDER funds in the framework of projects CTQ2012-33198, CSIC10-4E-805, and CSD2010-00024. S.M., F.P.-M and P.C. are also grateful to the European SUDOE TRAIN2 project and the Nanolito network through the MAT2011-13099-E project funded by the Ministry of Economy of Spain for supporting this collaborative work. S.M. also thanks his JIUZ-2013-CIE-05 grant. S.M. and P.C. acknowledge DGA and EU for funding Platon Research Group. R.J.N., P.J.L. and S.M.-G. thank EPSRC for funding (EP/K007785/1 and EP/K007548/1). P.J.L. held an EPSRC Leadership Fellowship, and currently holds an ARC Future Fellowship (FT120100073). L.M.B and J.C. acknowledge their grants from Banco Santander and MEC, respectively.

References

- [1] L. M. Ballesteros, S. Martín, C. Momblona, S. Marqués-González, M. C. López, R. J. Nichols, P. J. Low, P. Cea, *J. Phys. Chem. C* **2012**, *116*, 9142-9150.
- [2] M. I. Bruce, B. K. Nicholson, O. B. Shawkataly, *Inorg. Synth.* **1989**, *26*, 325.
- [3] G. Hogarth, M. M. Álvarez-Falcón, *Inorg. Chim. Acta* **2005**, *358*, 1386-1392.

- [4] S. Marqués-González, D. S. Yufit, J. A. K. Howard, S. Martín, H. M. Osorio, V. M. García-Suárez, R. J. Nichols, S. J. Higgins, P. Cea, P. J. Low, *Dalton Trans.* **2013**, 42, 338-341.
- [5] R. Uson, A. Laguna, M. Laguna, D. A. Briggs, H. H. Murray, J. P. Fackler, *Inorg. Synth.* **2007**, 26, 85-91.
- [6] P. Cea, C. Lafuente, J. S. Urieta, M. C. López, F. M. Royo, *Langmuir* **1996**, 12, 5881
- [7] S. Martín, P. Cea, C. Lafuente, F. M. Royo, M. C. López, *Surf. Sci.* **2004**, 563, 27-40.
- [8] V. W. W. Yam, K. L. Cheung, S. K. Yip, K. K. Cheung, *J. Org. Chem.* **2003**, 681, 196-209.
- [9] H. Schmidbaur, A. Schier, *Chem. Soc. Rev.* **2008**, 37, 1931-1951.
- [10] T. C. Liang, H. C. J. Lin, *J. Mater. Chem.* **2009**, 19, 4753-4763.
- [11] G. L. Gaines, *Insoluble monolayers at liquid-gas interface*, Interscience. John Wiley & Sons, New York, **1966**.
- [12] T. Classen, M. Lingenfelder, Y. Wang, R. Chopra, C. Virojanadara, U. Starke, G. Constantini, G. Fratesi, S. Fabris, S. de Gironcoli, S. Baroni, S. Haq, R. Raval, K. Kern, *J. Phys. Chem. A.* **2007**, 111, 12589-12603.
- [13] W. Liu, X. Yang, W. Huang, *J. Coll. Interf. Sci.* **2006**, 304, 160-165.
- [14] Y. C. Chang, *Appl. Surf. Sci.* **2011**, 257, 2401-2410.
- [15] L. Pranger, G. R., R. Tannenbaum, *Langmuir* **2005**, 21, 5396.
- [16] G. Liu, J. Liu, T. Böcking, P. K. Eggers, J. J. Gooding, *Chem. Phys.* **2005**, 136.
- [17] H.-G. Boyen, G. Kästle, F. Weigl, B. Koslowski, C. Dietrich, P. Ziemann, J. P. Spatz, S. Riethmüller, C. Hartmann, M. Möller, G. Schmid, M. G. Garnier, P. Oelhafen, *Science* **2002**, 297, 1533-1536.
- [18] C. Shan, H. Yang, D. Han, Q. Zhang, A. Ivaska, L. Niu, *Biosens. Bioelectron* **2010**, 25, 1070-1074.
- [19] G. Liu, E. Luais, J. J. Gooding, *Langmuir* **2011**, 27, 4176-4183.

- [20] M. C. Bourg, A. Badía, R. B. Lennox, *J. Phys. Chem. B.* **2000**, *104*, 6562-6567.
- [21] I. Fratoddi, I. Venditti, C. Battocchio, G. Polzonetti, C. Cametti, M. V. Russo, *Nanoscale Res. Lett.* **2011**, *6*, 98.
- [22] J. G. Simmons, *J. Appl. Phys.* **1963**, *281*, 1793-1803.